







Configurable pixelated skyrmions on nanoscale magnetic grids

Xichao Zhang ^{1,5}, Jing Xia ^{1,5}, Keiichiro Shirai¹, Hiroshi Fujiwara¹, Oleg A. Tretiakov ², Motohiko Ezawa ³✉, Yan Zhou ⁴✉ & Xiaoxi Liu ¹✉

Topological spin textures can serve as non-volatile information carriers. Here we study the current-induced dynamics of an isolated magnetic skyrmion on a nanoscale square-grid pinning pattern formed by orthogonal defect lines with reduced magnetic anisotropy. The skyrmion on the square grid can be pixelated with a quantized size of the grid. We demonstrate that the position, size, and shape of skyrmion on the square grid are electrically configurable. The skyrmion center is quantized to be on the grid and the skyrmion may show a hopping motion instead of a continuous motion. We find that the skyrmion Hall effect can be perfectly prohibited due to the pinning effect of the grid. The pixelated skyrmion can be harnessed to build future programmable racetrack memory, multistate memory, and logic computing device. Our results will be a basis for digital information storage and computation based on pixelated topological spin textures on artificial pinning patterns.

¹Department of Electrical and Computer Engineering, Shinshu University, 4-17-1 Wakasato, Nagano 380-8553, Japan. ²School of Physics, The University of New South Wales, Sydney 2052, Australia. ³Department of Applied Physics, The University of Tokyo, 7-3-1 Hongo, Tokyo 113-8656, Japan. ⁴School of Science and Engineering, The Chinese University of Hong Kong, Shenzhen, Guangdong 518172, China. ⁵These authors contributed equally: Xichao Zhang and Jing Xia. ✉email: ezawa@ap.t.u-tokyo.ac.jp; zhouyan@cuhk.edu.cn; liu@cs.shinshu-u.ac.jp

Topological spin textures in magnets are versatile objects that can be used to facilitate many magnetic and spintronic applications^{1–18}. The basic topological spin textures in magnets with Dzyaloshinskii-Moriya (DM) interactions are called magnetic skyrmions¹⁹, which have been created experimentally^{20–32} and suggested for use in spintronic functional devices, including memories^{33–41}, logic computing gates^{42–47}, field-effect transistors^{48–50}, memristors^{51,52}, and other novel applications^{53–60}.

Toward the realization of device applications based on skyrmions, a number of theoretical and experimental works have been devoted to the studies of statics and dynamics of skyrmions^{1–18}. In particular, the skyrmion texture is found to have several degrees of freedom that, in principle, could carry useful information and could be controlled and manipulated independently. For example, the position of a skyrmion can be manipulated by a spin current^{25,26,31,33–40,61–66}; the size of a skyrmion can be controlled by an out-of-plane magnetic field^{26–28,67}; the topological charge of a skyrmion can be changed by a vertical spin current⁶⁸; the polarity of a skyrmion can be switched by magnetic fields and spin currents^{69–72}; the helicity of a skyrmion in frustrated magnets can be manipulated by a spin current^{73–78}.

Typically, an isolated skyrmion stabilized by the DM interaction shows a circular shape^{19,67}. Recently, skyrmions with different shapes have been realized^{79–86}. For example, a square lattice of square-shaped skyrmions was discovered by Khanh et al.⁸⁰ in a centrosymmetric tetragonal magnet, of which the origin was theoretically investigated by Hayami and Motome⁸¹. A square lattice of square-shaped antiskyrmions was also observed experimentally by Peng et al.⁸² in a noncentrosymmetric magnet. Besides, it is found that skyrmions and antiskyrmions can show elliptical shapes in samples with anisotropic DM interactions^{83–85}. The deformation of a skyrmion induced by external forces may also result in a non-circular shape^{31,65}. All these findings on skyrmions showing different shapes reflect the importance of controlling the shape of a skyrmion, which may lead to novel spintronic applications based on topological spin textures with different shapes.

Recently, Juge et al.⁸⁷ and Ohara et al.⁸⁸ independently demonstrated the control of skyrmion position by locally modifying the magnetic properties. They experimentally realized the confinement of skyrmions in nanoscale tracks with modified magnetic properties on a large film. In particular, the local modification of perpendicular magnetic anisotropy (PMA) can result in an energy barrier, which plays a key role on the confinement and pinning of skyrmions. Therefore, by locally modifying PMA or other magnetic properties it is envisioned that one can fabricate different types of artificial pinning patterns on magnetic materials, such as parallel defect lines, grids, and square patterns^{18,86,89–109}. These artificial pinning patterns may lead to very special static and dynamic behaviors of topological spin textures interacting with them^{18,86,89–109}. For example, the skyrmion Hall effect can be controlled or reduced for skyrmions moving over two-dimensional periodic pinning arrays in certain cases^{91,105}. Moreover, the artificial pinning patterns would also offer the possibility to study basic science issues since particles and quasi-particles (e.g., superconducting vortices and colloids) on periodic substrates is a wide-ranging problem^{18,110–116}.

In this work, we report the properties of a skyrmion in a magnetic thin film with the square-grid pinning pattern formed by nanoscale orthogonal defect lines with reduced PMA. We show that the square grid leads to the formation of pixelated skyrmions, of which the position and area are quantized in the unit of the grid cell. We find that the position, size, and shape of a pixelated skyrmion can be manipulated precisely by a current pulse.

Results and discussion

Static properties of the square-shaped skyrmion. Figure 1 (a) depicts the simulation geometry. We consider a ferromagnetic (FM) thin layer attached to a heavy-metal layer, where the FM layer has certain PMA and interface-induced DM interaction. The FM layer thickness is fixed at 1 nm in all simulations. We assume that the square-grid pinning pattern in the FM layer is formed by orthogonal defect lines with reduced PMA, which can be realized in experiments by locally modifying the magnetic properties (i.e., using additional sputtered layers or ion

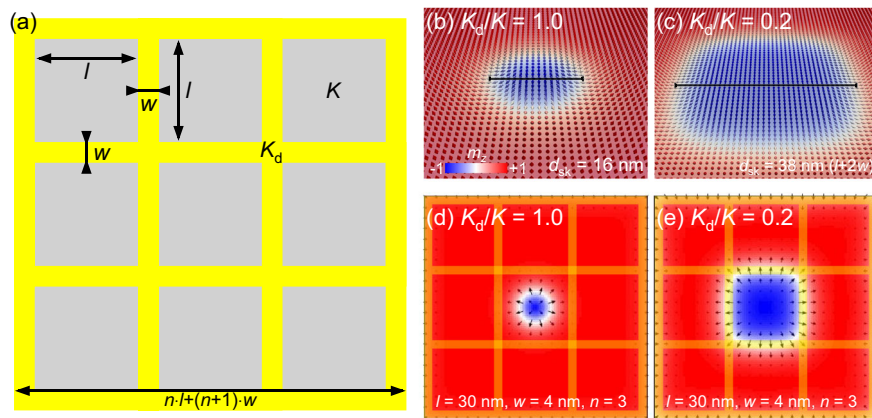


Fig. 1 An ordinary magnetic skyrmion and a square-shaped magnetic skyrmion. **a** Top-view schematic of the simulation geometry. l denotes the spacing between two adjacent parallel defect lines. w denotes the width of the defect line. n denotes the number of unit square patterns along the x and y directions. The total side length of the ferromagnetic layer equals $n \cdot l + (n + 1) \cdot w$. K and K_d stand for the perpendicular magnetic anisotropy constants for the unmodified areas and defect lines, respectively. The defect lines with reduced K_d are indicated by yellow lines. The thickness of the ferromagnetic layer is fixed at 1 nm. **b** Illustration of a relaxed ordinary round-shaped skyrmion with the topological charge of $Q = 1$ at the center of a sample with $K_d/K = 1$. The side length of the sample equals 106 nm. The relaxed skyrmion diameter d_{sk} equals 16 nm, which is indicated by the black line. The color scale represents the out-of-plane magnetization component m_z , which has been used throughout the work. **c** Illustration of a relaxed square-shaped skyrmion with $Q = 1$ at the center of a sample with $K_d/K = 0.2$. Here, $l = 30$ nm, $w = 4$ nm, and $n = 3$. The side length of the sample equals 106 nm. The relaxed skyrmion diameter d_{sk} equals 38 nm, as indicated by the black line. **d** Top view of the sample with $K_d/K = 1$, corresponding to **(b)**. **e** Top view of the sample with $K_d/K = 0.2$, corresponding to **(c)**.

irradiation)^{87,88,117}. The width of each defect line is defined as w . The distance between two nearest-neighboring parallel defect lines is defined as l . The number of unit square patterns along the x or y directions is defined as n . Hence, the total side length of the FM layer is equal to $nl + (n + 1)w$ [see Fig. 1(a)]. The magnetic parameters and other modeling details are given in the Methods.

We first study a static single isolated skyrmion in the sample with the square grid. At the initial state, a Néel-type skyrmion with a theoretical topological charge $Q = 1$ is placed at the sample center, which is relaxed to a stable or metastable state by the OOMMF conjugate gradient minimizer¹¹⁸. The topological charge Q is defined as $Q = -\frac{1}{4\pi} \int \mathbf{m} \cdot (\frac{\partial \mathbf{m}}{\partial x} \times \frac{\partial \mathbf{m}}{\partial y}) dx dy$ with \mathbf{m} being the reduced magnetization. In this work, we assume that the initial skyrmion diameter is smaller than the defect-line spacing l . For example, the relaxed ordinary skyrmion has a diameter d_{sk} of 16 nm in the sample with $l = 30$ nm, $w = 4$ nm, $n = 3$, and $K_d/K = 1$ [see Fig. 1(b)]. $K_d/K = 1$ means no square-grid pinning pattern exists in the sample. However, when $K_d/K < 1$, the initial skyrmion may relax to a square-shaped skyrmion with an enlarged size determined by the square-grid pinning pattern, as shown in Fig. 1(c). In particular, the diameter (i.e., the side length) of the square-shaped skyrmion d_{sk} is found to be $l + 2w$. For example, in Fig. 1(c) the relaxed square-shaped skyrmion shows $d_{sk} = 38$ nm in the sample with $l = 30$ nm, $w = 4$ nm, $n = 3$, and $K_d/K = 0.2$. We note that the square-shaped skyrmion with a larger size will be easier to be detected and observed. Once a square-shaped skyrmion is formed on the grid, its position and area are determined in the unit of the grid cell. As a minute grid cell is regarded as a pixel of the grid, the square-shaped skyrmion on the grid is seen as a pixelated skyrmion with quantized area.

Figure 1 (d),(e) show the top views of an ordinary skyrmion at $K_d/K = 1$ and a square-shaped skyrmion at $K_d/K = 0.2$, respectively. The formation of the square-shaped skyrmion on the grid with $K_d/K < 1$ is due to the fact that the defect line with reduced PMA attracts the domain wall or skyrmion near it⁸⁸. The formation of the square-shaped skyrmion is favored by smaller K_d/K and wider defect lines provided that $0 \leq K_d/K \leq 1$ and $w \ll d_{sk} < l$ (see Supplementary Note 1). We note that the square-shaped skyrmion is formed on the grid in the absence of an out-of-plane magnetic field B_z . However, the size of the square-shaped skyrmion is adjusted by B_z when K_d is much smaller than K (see Supplementary Note 2).

Current-induced dynamics of the square-shaped skyrmion. We also study the current-induced dynamics of a square-shaped skyrmion on the grid (see Fig. 2). We consider a sample at $B_z = 0$ mT with $l = 30$ nm, $w = 4$ nm, and $n = 11$. The total side length of the sample is equal to 378 nm. At the initial state (i.e., $t = 0$ ps), we place a relaxed skyrmion with $Q = 1$ at the sample center. We first apply a single current pulse to drive the dynamics at a damping parameter of $\alpha = 0.3$. The pulse length is fixed at $\tau = 400$ ps. The current density is fixed at $j = 100$ MA cm⁻². After the application of the pulse, the sample is relaxed for 600 ps. The total simulation time equals 1000 ps. Note that we only consider the damping-like spin-orbit torque generated by the current pulse (see Methods). The field-like torque contribution in our material system could be very small compared to the damping-like torque as our system does not have a large interfacial Rashba effect. Also, a large field-like torque usually leads to the deformation of a skyrmion⁶⁵, which cannot provide a driving force.

As shown in Fig. 2(a), an ordinary skyrmion shows directional motion in the sample with $K_d/K = 1$ when a single current pulse is applied. The direction of motion depends on the spin

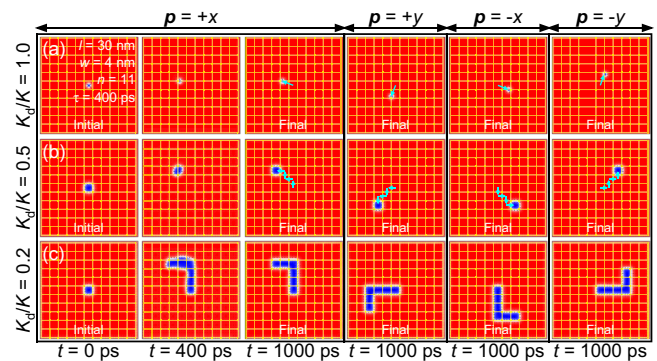


Fig. 2 Current-induced dynamics of a square-shaped skyrmion on the grids. **a** Top views of the current-induced motion of an ordinary round-shaped skyrmion in a sample with $K_d/K = 1$ for different spin polarization direction \mathbf{p} . K and K_d stand for the perpendicular magnetic anisotropy constants for the unmodified areas and defect lines, respectively. The side length of the sample equals 378 nm. An ordinary skyrmion with the topological charge of $Q = 1$ is relaxed at the sample center as the initial state at $t = 0$ ps. A 400-ps-long current pulse of $j = 100$ MA cm⁻² is applied, and then the system is relaxed for 600 ps. Here the damping parameter $\alpha = 0.3$. **b** Top views of the current-induced hopping motion of a square-shaped skyrmion in a sample with defect lines for different \mathbf{p} . Here, $l = 30$ nm, $w = 4$ nm, $n = 11$, and $K_d/K = 0.5$. l denotes the spacing between two adjacent parallel defect lines. w denotes the width of the defect line. n denotes the number of unit square patterns along the x and y directions. The side length of the sample equals 378 nm. A square-shaped skyrmion with $Q = 1$ is relaxed at the sample center as the initial state at $t = 0$ ps. A 400-ps-long current pulse of $j = 100$ MA cm⁻² is applied, and then the system is relaxed for 600 ps. The defect lines with reduced K_d are indicated by yellow lines. The motion route is denoted by the cyan arrow. **c** Top views of the current-induced deformation of a square-shaped skyrmion in a sample with defect lines for different \mathbf{p} . Here $K_d/K = 0.2$. The other parameters are the same as those in (b).

polarization direction \mathbf{p} , which is controlled by the current injection direction in experiments. When $\mathbf{p} = +\hat{x}$, the ordinary skyrmion moves smoothly toward the $+y$ direction and shows an obvious transverse shift in the $-x$ direction due to the skyrmion Hall effect^{64,65}. The skyrmion stops when the current pulse is off at $t = \tau = 400$ ps, and the final state obtained at $t = 1000$ ps shows that the skyrmion is closer to the upper left corner of the sample (see Supplementary Movie 1). The skyrmion moves closer to the lower left, lower right, and upper right corners driven by the current pulses with $\mathbf{p} = +\hat{y}$, $\mathbf{p} = -\hat{x}$, and $\mathbf{p} = -\hat{y}$, respectively.

When $K_d/K < 1$, we find that the square-shaped skyrmion shows very different current-induced dynamic behaviors, which depend on the value of K_d/K . In the sample with $K_d/K = 0.5$, the square-shaped skyrmion shows a hopping motion instead of a smooth motion [see Fig. 2(b)], which is caused by the pinning effect of the grid (see Supplementary Movie 2). The hopping motion toward the sample corner is a result of the skyrmion Hall effect. However, in the sample with $K_d/K = 0.2$, the square-shaped skyrmion shows directional elongation and deformation when the current pulse is applied [see Fig. 2(c)]. Due to the skyrmion Hall effect, the square-shaped skyrmion is transformed to a pixelated L-shaped skyrmion (see Supplementary Movie 3), which carries a theoretical topological charge of $Q = 1$. We find that depending on \mathbf{p} , the position and orientation of the final L-shaped skyrmion can be controlled.

First, we review the results on an ordinary skyrmion with $K_d/K = 1$. m_z slightly decreases to a stable value during the application of the current pulse, indicating the steady motion of the skyrmion with a slightly reduced size during the pulse application as shown in

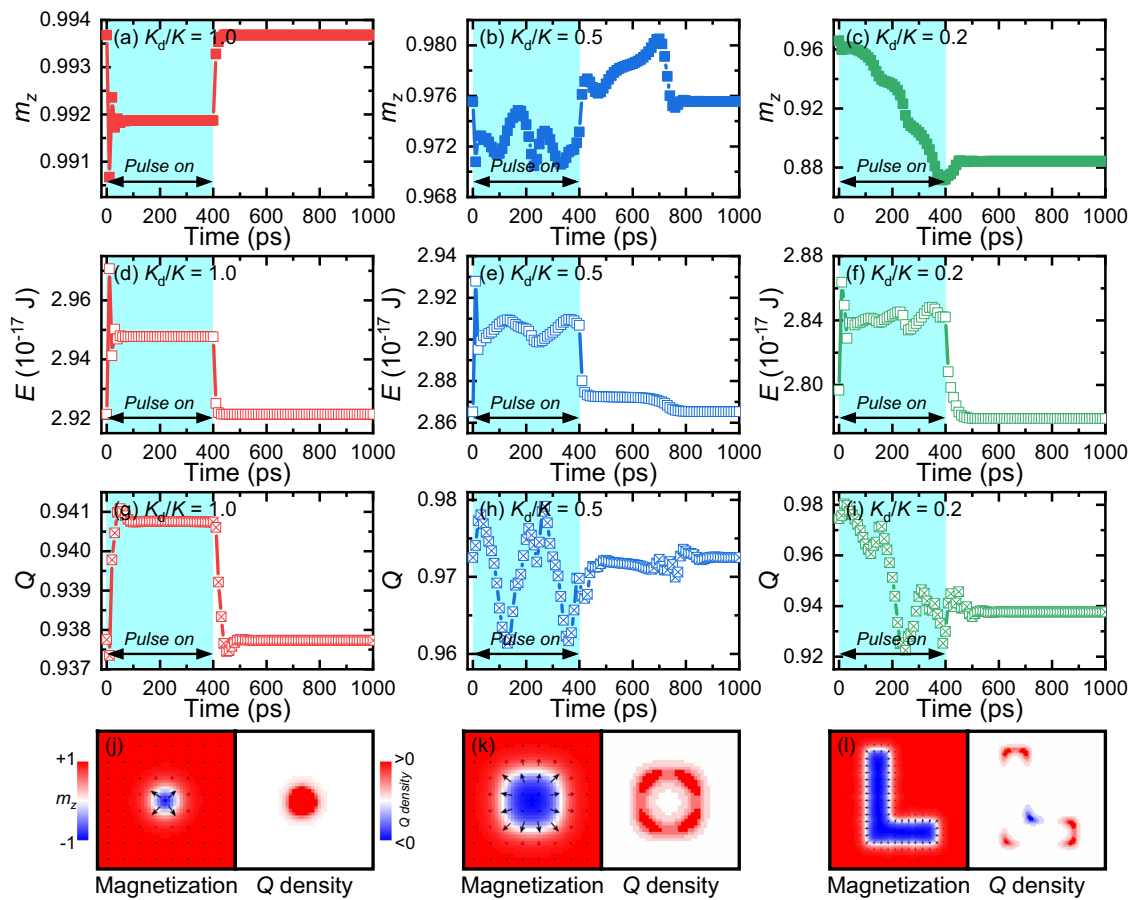


Fig. 3 Out-of-plane magnetization, energy, and topological charge of the current-driven square-shaped skyrmion. **a** Time-dependent out-of-plane magnetization m_z corresponding to the current-induced motion of an ordinary round-shaped skyrmion in a sample with $K_d/K = 1$. K and K_d stand for the perpendicular magnetic anisotropy constants for the unmodified areas and defect lines, respectively. A 400-ps-long current pulse of $j = 100 \text{ MA cm}^{-2}$ and $\mathbf{p} = +\hat{x}$ is applied, and then the system is relaxed for 600 ps. **b** Time-dependent m_z corresponding to the current-induced hopping motion of a square-shaped skyrmion in a sample with defect lines of $K_d/K = 0.5$. **c** Time-dependent m_z corresponding to the current-induced deformation of a square-shaped skyrmion in a sample with defect lines of $K_d/K = 0.2$. **d** Time-dependent total energy E of the system corresponding to (a). **e** Time-dependent E corresponding to (b). **f** Time-dependent E corresponding to (c). **g** Time-dependent numerical topological charge Q of the system corresponding to (a). **h** Time-dependent numerical Q corresponding to (b). **i** Time-dependent numerical Q corresponding to (c). **j** Q density distribution of an ordinary skyrmion. **k** Q density distribution of a square-shaped skyrmion. **l** Q density distribution of an L-shaped skyrmion at the final state.

Fig. 3(a). The time-dependent total energy E is given in Fig. 3(d), which rapidly recovers to the initial-state value after the pulse application, suggesting that the initial and final states are the same. Figure 3(g) shows the time-dependent numerical topological charge Q , which slightly increases during the skyrmion motion. We note that the numerical Q is not exactly equal to 1 at the initial and final state. The non-integer value is caused by the discretized meshes and the current-induced deformation of the skyrmion. We have excluded the effect of tilted edge spins on the calculation of Q .

Next, we study the case with $K_d/K = 0.5$, where a square-shaped skyrmion shows a hopping motion. m_z oscillates during the pulse application, which implies the oscillating changes of the skyrmion size and shape during its hops across square grid cells as shown in Fig. 3(b). The detailed process is shown in Fig. 4(c). After the pulse application, both m_z and E are recovered to their initial-state values at $t = 0$ ps [see Fig. 3(e)], justifying that the initial and final skyrmion states are the same because of the translational symmetry of the square-shaped skyrmion. We note that the numerical Q oscillates during the pulse application [see Fig. 3(h)], which is caused by the oscillation of the square-shaped skyrmion.

Finally, we study the case with $K_d/K = 0.2$. As the square-shaped skyrmion is enlarged and deformed during the pulse

application, m_z significantly decreases during $t = 0 - 400$ ps and reaches a stable value at $t = 500$ ps. See Fig. 3(c). The detailed process is shown in Fig. 4(d). E increases and oscillates during the deformation [see Fig. 3(f)], indicating the deformation is produced by overcoming periodic energy barriers on the grid. The numerical Q oscillates and slightly decreases [see Fig. 3(i)], which result from the different sizes and shapes of the initial and final states. The distributions of local Q density for the ordinary, square-shaped, and L-shaped skyrmions are given in Fig. 3(j),(k),(l), respectively. We find that the local Q density is localized at the corners of pixelated skyrmions. Especially, the local Q density is negative for the 270 degree corner of the L-shaped skyrmion.

In Fig. 4, we continue to investigate the effect of the pulse length τ on the dynamics of a square-shaped skyrmion. At $t = 0$ ps, we place a relaxed square-shaped skyrmion with $Q = 1$ at the sample center. We focus on the dynamics induced by a single current pulse with $j = 100 \text{ MA cm}^{-2}$ and $\mathbf{p} = -\hat{y}$. As shown in Fig. 4(a), the square-shaped skyrmion in the sample with $K_d/K = 0.5$ hops from the grid cell at the sample center to the right nearest-neighboring grid cell after the pulse application with $\tau = 100$ ps (see Supplementary Movie 4). It shows no transverse shift because that the applied current pulse is too short to activate

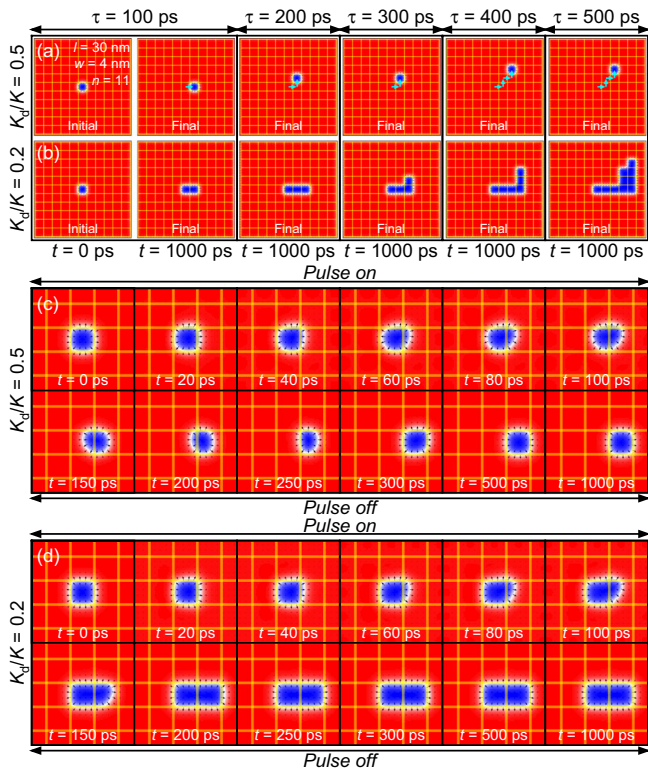


Fig. 4 Effect of pulse length on the current-induced dynamics of a square-shaped skyrmion. **a** Top views of the hopping motion of a square-shaped skyrmion driven by a current pulse with the pulse length τ . Here, $l = 30$ nm, $w = 4$ nm, $n = 11$, $K_d/K = 0.5$, and the damping parameter $\alpha = 0.3$. K and K_d stand for the perpendicular magnetic anisotropy constants for the unmodified areas and defect lines, respectively. l denotes the spacing between two adjacent parallel defect lines. w denotes the width of the defect line. n denotes the number of unit square patterns along the x and y directions. The side length of the sample equals 378 nm. A square-shaped skyrmion with the topological charge of $Q = 1$ is relaxed at the sample center as the initial state at $t = 0$ ps. A current pulse of $j = 100$ MA cm $^{-2}$ and $\mathbf{p} = -\hat{y}$ is applied, and then the system is relaxed until $t = 1000$ ps. The defect lines with reduced K_d are indicated by yellow lines. The motion route is denoted by the cyan arrow. **b** Top views of the deformation of a square-shaped skyrmion driven by a current pulse with τ . Here $K_d/K = 0.2$. The other parameters are the same as those in **(a)**. **c** Zoomed top views of the hopping motion of a square-shaped skyrmion driven by a 100-ps-long pulse of $j = 100$ MA cm $^{-2}$. The other parameters are the same as those in **(a)**. **d** Zoomed top views of the deformation of a square-shaped skyrmion driven by a 100-ps-long pulse of $j = 100$ MA cm $^{-2}$. The other parameters are the same as those in **(b)**.

the skyrmion Hall effect, as shown in Fig. 4(c). Therefore, by applying a sequence of 100-ps-long pulses with a pulse spacing of 900 ps, it is possible to drive the square-shaped skyrmion moves exactly toward the $+x$ direction without showing the skyrmion Hall effect (see Supplementary Movie 5). When $\tau = 200 - 500$ ps, the square-shaped skyrmion shows the skyrmion Hall effect during its hopping motion (see Supplementary Movie 6).

In Fig. 4(b), the square-shaped skyrmion in the sample with $K_d/K = 0.2$ elongates to a rectangle-shaped skyrmion after the pulse application with $\tau = 100 - 200$ ps (see Supplementary Movie 7). As mentioned above, a part of the domain wall forming the skyrmion is pinned by the defect line. Hence, the square-shaped skyrmion is forced to deform along the $+x$ direction when the skyrmion Hall effect is prohibited [see Fig. 4(d)]. However, under the pulse application with $\tau = 300 - 400$ ps, the depinned

domain wall tends to propagate in both the $+x$ and $+y$ directions due to the skyrmion Hall effect; therefore, the square-shaped skyrmion is deformed into an L-shaped skyrmion (see Supplementary Movie 8), which is regarded as an L-shaped skyrmion as it carries a theoretical $Q = 1$. When $\tau = 500$ ps, the deformation is more remarkable and complex, leading to an abnormal L-shaped skyrmion.

In Fig. 5(a), we show the time-evolution of m_z corresponding to the hopping motion for various τ with $K_d/K = 0.5$. m_z oscillates with time upon the pulse application and recovers to its initial value soon after the pulse application. Such a feature of m_z signal can be utilized to electrically detect the hopping motion of skyrmion. E increases and varies with time in a regular way during the pulse application [see Fig. 5(c)], implying the skyrmion moves regularly on the grid. The variation of the numerical Q is directly related to the skyrmion deformation [see Fig. 5(e)]. Next, we study the case with $K_d/K = 0.2$. Both m_z and E are decreased after the pulse application [see Fig. 5(b) and (d)], which indicates the rectangle-shaped and L-shaped skyrmions are stabler. It is noteworthy that the topological nature of the skyrmion remains unchanged after its deformation [see Fig. 5(f)]. Since the area of a skyrmion on the grid is an integer multiple of the minimum grid cell area, the E distribution of all possible pixelated skyrmions on the grid is discontinuous.

We also study the effects of j and α on the dynamics of a square-shaped skyrmion (see Supplementary Note 3). The effect of j is similar to that of τ . A large α will reduce the skyrmion Hall effect for the skyrmion hop and deformation, which leads to the current-induced formation of the rectangle-shaped skyrmion. A basic phase diagram of the system transitions from the single skyrmion hopping to the skyrmion deformation is given in Fig. 6. We point out four possible cases induced by the current pulses with different pulse lengths. First, for the samples with relatively stronger pinning strengths ($K_d/K < 0.5$), a weak current pulse cannot drive the square-shaped skyrmion. Namely, the square-shaped skyrmion is pinned at its initial position during and after the pulse application. For a strong current pulse, the square-shaped skyrmion will be transformed to a rectangle-shaped skyrmion by the current pulse. Second, for the sample with a moderate pinning strength ($K_d/K = 0.5$), a weak current pulse cannot drive the square-shaped skyrmion, but a stronger current pulse may drive the square-shaped skyrmion into a hopping motion or shrinking. Third, for the sample with relatively weaker pinning strength ($K_d/K > 0.5$), the square-shaped skyrmion may not be stable on the square pinning pattern. Hence, once a current pulse is applied, the square-shaped skyrmion will first depin and then shrink to a smaller round-shaped skyrmion. Such a smaller round-shaped skyrmion could be pinned again on the defect line after the pulse application.

Conclusions

In conclusion, we have studied the statics and dynamics of configurable skyrmions on the grid formed by orthogonal defect lines with identical spacings and reduced PMA. We find that the grid results in the pixelation of skyrmions, leading to the square-shaped, rectangle-shaped, and L-shaped skyrmions. The position and area of the square-shaped skyrmion are quantized in the unit of the grid cell, which are different to ordinary skyrmions, of which the position and size change continuously.

We numerically demonstrate that the position, size, and shape of a square-shaped skyrmion on the grid are manipulated electrically, which depend on the pinning strength, the applied current pulse, and the damping parameter. In particular, we show that the square-shaped skyrmion hops on the grid with weak pinning, and its skyrmion Hall effect can be controlled by the

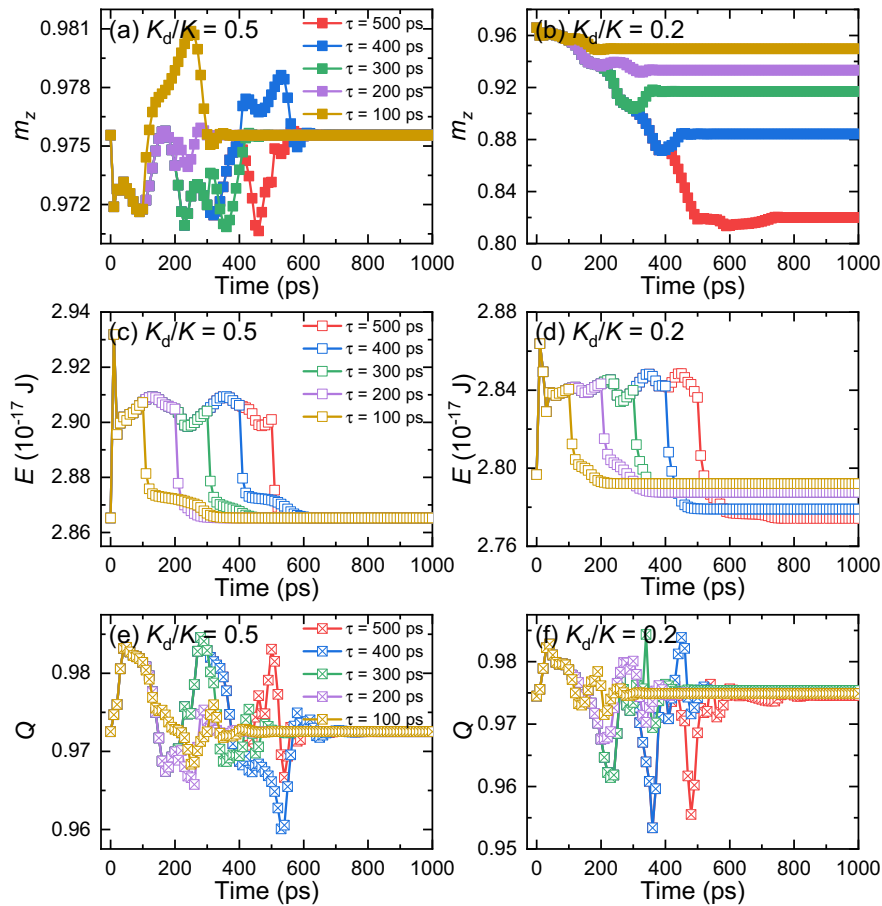


Fig. 5 Out-of-plane magnetization, energy, and topological charge of the system driven by current pulses with different pulse lengths. **a** Time-dependent out-of-plane magnetization m_z corresponding to the current-induced hopping motion of a square-shaped skyrmion in a sample with $K_d/K = 0.5$ for different pulse lengths τ . K and K_d stand for the perpendicular magnetic anisotropy constants for the unmodified areas and defect lines, respectively. A current pulse of $j = 100 \text{ MA cm}^{-2}$ and $\mathbf{p} = -\hat{y}$ is applied, and then the system is relaxed until $t = 1000 \text{ ps}$. **b** Time-dependent out-of-plane magnetization m_z corresponding to the current-induced deformation of a square-shaped skyrmion in a sample with $K_d/K = 0.2$ for different τ . **c** Time-dependent total energy E of the system corresponding to **(a)**. **(d)** Time-dependent E corresponding to **(b)**. **e** Time-dependent numerical topological charge Q of the system corresponding to **(a)**. **f** Time-dependent numerical Q corresponding to **(b)**.

current pulse. Especially, the skyrmion Hall effect of the square-shaped skyrmion is perfectly prohibited by appropriately tuning parameters. The straight hopping motion of skyrmion is vital for racetrack-type memory devices. The control of the skyrmion Hall effect using a preset sequence of current pulses provides the possibility to build a logic computing device based on the transport route of skyrmions. In addition, it is possible to reduce the width of a nanotrack as wide as three grid cells since the skyrmion Hall effect is suppressed. It is highly contrasted with the case of an ordinary skyrmion, where we need to use a wider nanotrack in order to keep away a skyrmion from an edge. It is possible to shift a skyrmion by N grid cells by applying N pulses since the skyrmion relaxes to the same structure only by changing its position after the pulse is over.

Besides, we find that the current pulse drives the square-shaped skyrmion to deform on the square grid with strong pinning, which transforms the square-shaped skyrmion to a rectangle-shaped or L-shaped skyrmion in a controlled manner. It can be utilized to build a multistate memory⁴¹ or an artificial synapse⁵⁹ based on different metastable topological spin textures in one sample, where topological spin textures with different m_z stand for different states that can be detected by measuring magnetoresistance. It is worth mentioning that a reset function, that is, a method to transform an L-shaped skyrmion to an original square-shaped skyrmion may be required for the multistate

memory and artificial synapse applications. Such a reset function can be achieved by applying an out-of-plane magnetic field pulse in our system (see Supplementary Note 4). Indeed, one can also reset the system by erasing the entire state and then nucleate a square-shaped skyrmion.

Our results give a deeper understanding of the complex dynamics of a skyrmion on a nanoscale grid formed by defect lines with modified magnetic anisotropy. It will be straightforward to generalize our results to the systems with artificial nanoscale triangular and honeycomb grids. However, the square-grid pinning pattern is most efficient to prohibit the skyrmion Hall effect and easily manufacturable, which is due to the fact that a typical lithography scanner system works in a way that favors horizontal and vertical scanning directions. For this reason, the fabrication of the triangular or irregular shape may result in obvious polygon edges. Such an effect may significantly reduce the pinning pattern quality when the resolution goes down to a few nanometers. Hence, the square-grid pinning pattern and rectangle-grid pinning pattern (see Supplementary Note 5) may be the most reliable choices. Besides, the advantage of using the square-grid pinning pattern to guide the skyrmion motion is that the skyrmion can be delivered toward different directions by controlling the driving current direction, current density, and pulse length. Such a feature may not be possible on other pinning patterns such as the parallel defect lines.

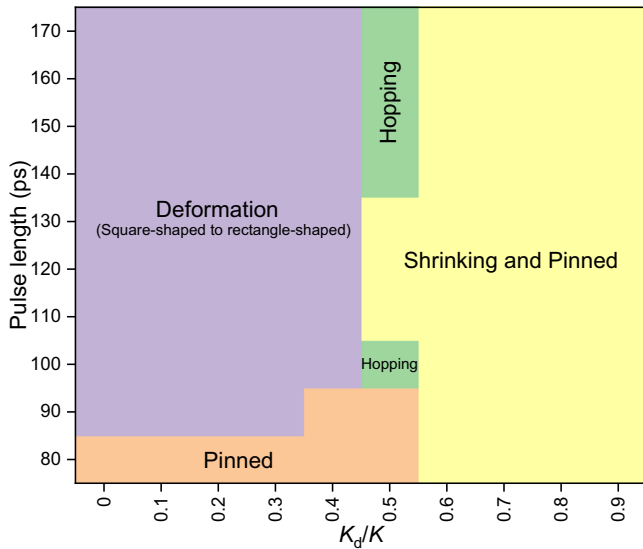


Fig. 6 A basic phase diagram of the system transitions from single skyrmion hopping to the skyrmion deformation. Deformation means the square-shaped skyrmion is deformed to a rectangle-shaped skyrmion after the pulse application. Hopping means the square-shaped skyrmion hops from the grid cell at the sample center to the right nearest-neighboring grid cell after the pulse application. Pinned means the square-shaped skyrmion is pinned by the grid cell at the sample center during and after the pulse application. Shrinking and pinned means the square-shaped skyrmion shrinks to a smaller round-shaped skyrmion and is pinned on the defect line after the pulse application. Here, $l = 30$ nm, $w = 4$ nm, $n = 11$, and the damping parameter $\alpha = 0.3$. l denotes the spacing between two adjacent parallel defect lines. w denotes the width of the defect line. n denotes the number of unit square patterns along the x and y directions. The side length of the sample equals 378 nm. A square-shaped skyrmion with the topological charge of $Q = 1$ is relaxed at the sample center as the initial state at $t = 0$ ps. A current pulse of $j = 100$ MA cm $^{-2}$ and $\mathbf{p} = -\hat{y}$ is applied, and then the system is relaxed until $t = 1000$ ps. The final states are confirmed at $t = 1000$ ps.

On the other hand, we would like to point out that the square-grid pinning pattern could also serve as a platform for the study of multiple skyrmions interacting with a pinning landscape (see Supplementary Note 6), and a great many directions one could go with this system such as different kinds of driving forces¹⁸. Last, from the point of view of electronic device applications, future works on this topic may focus on the performance analysis, such as the energy expenditures of skyrmion hopping and square-to-L deformation. Our results may provide guidelines for building spintronic applications utilizing the interaction between topological spin textures and artificial pinning patterns.

Methods

Micromagnetic simulations. All spin relaxation and dynamics simulations are carried out by using the Object Oriented MicroMagnetic Framework (OOMMF) developed at NIST¹⁸. The three-dimensional spin dynamics in the FM sample is governed by the Landau-Lifshitz-Gilbert (LLG) equation augmented with the damping-like spin-orbit torque¹⁸

$$\frac{d\mathbf{M}}{dt} = -\gamma_0 \mathbf{M} \times \mathbf{H}_{\text{eff}} + \frac{\alpha}{M_S} \left(\mathbf{M} \times \frac{d\mathbf{M}}{dt} \right) + \frac{u}{M_S} (\mathbf{M} \times \mathbf{p} \times \mathbf{M}), \quad (1)$$

where the damping-like spin torque is generated through the spin Hall effect in the heavy-metal layer when an electric current is injected³⁵. In Eq. (1), \mathbf{M} is the magnetization, $M_S = |\mathbf{M}|$ is the saturation magnetization, t is the time, γ_0 is the absolute value of gyromagnetic ratio, α is the Gilbert damping parameter, and $\mathbf{H}_{\text{eff}} = -\mu_0^{-1} \partial \epsilon / \partial \mathbf{M}$ is the effective field. $u = |(\gamma_0 \hbar) / (\mu_0 e)| \cdot (j \theta_{\text{SH}}) / (2aM_S)$ is the spin torque coefficient, \mathbf{p} stands for the unit spin polarization direction, μ_0 is the

vacuum permeability constant, \hbar is the reduced Planck constant, e is the electron charge, j is the driving current density, and θ_{SH} is the spin Hall angle.

The average energy density ϵ contains the PMA, FM exchange, demagnetization, applied magnetic field, and interface-induced DM interaction energy terms, given as

$$\epsilon = -K \frac{(\mathbf{n} \cdot \mathbf{M})^2}{M_S^2} + A \left[\nabla \left(\frac{\mathbf{M}}{M_S} \right) \right]^2 - \frac{\mu_0}{2} \mathbf{M} \cdot \mathbf{H}_d - \mathbf{M} \cdot \mathbf{B} + \frac{D}{M_S} [M_z (\mathbf{M} \cdot \nabla) - (\nabla \cdot \mathbf{M}) M_z], \quad (2)$$

where K , A , and D are the PMA, FM exchange, and DM interaction energy constants, respectively. \mathbf{B} is the applied magnetic field, and \mathbf{H}_d is the demagnetization field. \mathbf{n} is the unit surface normal vector. M_z is the out-of-plane component of \mathbf{M} . The default parameters used in this work are^{34,35,38}: $\gamma_0 = 2.211 \times 10^5$ m A $^{-1}$ s $^{-1}$, $\alpha = 0.05 \sim 0.5$, $M_S = 580$ kA m $^{-1}$, $K = 0.8$ MJ m $^{-3}$, $A = 15$ pJ m $^{-1}$, $D = 3$ mJ m $^{-2}$, and $\theta_{\text{SH}} = 0.2$. The mesh size is set as $1 \times 1 \times 1$ nm 3 in all simulations, guaranteeing both accuracy and efficiency.

Data availability

The data that support the findings of this study are available from the corresponding authors upon reasonable request.

Code availability

The micromagnetic simulator OOMMF used in this work is publicly accessible at <http://math.nist.gov/oommf>.

Received: 2 August 2021; Accepted: 10 November 2021;

Published online: 02 December 2021

References

- Nagaosa, N. & Tokura, Y. Topological properties and dynamics of magnetic skyrmions. *Nat. Nanotechnol.* **8**, 899 (2013).
- Mochizuki, M. & Seki, S. Dynamical magnetoelectric phenomena of multiferroic skyrmions. *J. Phys.: Condens. Matter* **27**, 503001 (2015).
- Wiesendanger, R. Nanoscale magnetic skyrmions in metallic films and multilayers: a new twist for spintronics. *Nat. Rev. Mater.* **1**, 16044 (2016).
- Finocchio, G., Büttner, F., Tomasello, R., Carpentieri, M. & Kläui, M. Magnetic skyrmions: from fundamental to applications. *J. Phys. D: Appl. Phys.* **49**, 423001 (2016).
- Kang, W., Huang, Y., Zhang, X., Zhou, Y. & Zhao, W. Skyrmion-Electronics: an overview and outlook. *Proc. IEEE* **104**, 2040 (2016).
- Kanazawa, N., Seki, S. & Tokura, Y. Noncentrosymmetric magnets hosting magnetic skyrmions. *Adv. Mater.* **29**, 1603227 (2017).
- Jiang, W. et al. Skyrmions in magnetic multilayers. *Phys. Rep.* **704**, 1 (2017).
- Fert, A., Reyren, N. & Cros, V. Magnetic skyrmions: advances in physics and potential applications. *Nat. Rev. Mater.* **2**, 17031 (2017).
- Everschor-Sitte, K., Masell, J., Reeve, R. M. & Kläui, M. Perspective: magnetic skyrmions - Overview of recent progress in an active research field. *J. Appl. Phys.* **124**, 240901 (2018).
- Zhou, Y. Magnetic skyrmions: intriguing physics and new spintronic device concepts. *Natl. Sci. Rev.* **6**, 210 (2019).
- Diep, H. T. Phase transition in frustrated magnetic thin film - Physics at phase boundaries. *Entropy* **21**, 175 (2019).
- Zhang, X. et al. Skyrmion-electronics: Writing, deleting, reading and processing magnetic skyrmions toward spintronic applications. *J. Phys.: Condens. Matter* **32**, 143001 (2020).
- Göbel, B., Mertig, I. & Tretiakov, O. A. Beyond skyrmions: review and perspectives of alternative magnetic quasiparticles. *Phys. Rep.* **895**, 1 (2021).
- Back, C. et al. The 2020 skyrmionics roadmap. *J. Phys. D: Appl. Phys.* **53**, 363001 (2020).
- Bogdanov, A. N. & Panagopoulos, C. Physical foundations and basic properties of magnetic skyrmions. *Nat. Rev. Phys.* **2**, 492 (2020).
- Li, S. et al. Magnetic skyrmions for unconventional computing. *Mater. Horiz.* **8**, 854 (2021).
- Luo, S. & You, L. Skyrmion devices for memory and logic applications. *APL Mater.* **9**, 050901 (2021).
- Reichhardt, C., Reichhardt, C. J. O. & Milosevic, M. V. Statics and dynamics of skyrmions interacting with pinning: a review, *arXiv:2102.10464* (2021).
- Rößler, U. K., Bogdanov, A. N. & Pfleiderer, C. Spontaneous skyrmion ground states in magnetic metals. *Nature* **442**, 797 (2006).
- Mühlbauer, S. et al. Skyrmion lattice in a chiral magnet. *Science* **323**, 915 (2009).
- Yu, X. Z. et al. Real-space observation of a two-dimensional skyrmion crystal. *Nature* **465**, 901 (2010).

22. Heinze, S. et al. Spontaneous atomic-scale magnetic skyrmion lattice in two dimensions. *Nat. Phys* **7**, 713 (2011).
23. Schulz, T. et al. Emergent electrodynamics of skyrmions in a chiral magnet. *Nat. Phys* **8**, 301 (2012).
24. Romming, N. et al. Writing and deleting single magnetic skyrmions. *Science* **341**, 636 (2013).
25. Jiang, W. et al. Blowing magnetic skyrmion bubbles. *Science* **349**, 283 (2015).
26. Woo, S. et al. Observation of room-temperature magnetic skyrmions and their current-driven dynamics in ultrathin metallic ferromagnets. *Nat. Mater* **15**, 501 (2016).
27. Moreau-Lucaire, C. et al. Additive interfacial chiral interaction in multilayers for stabilization of small individual skyrmions at room temperature. *Nat. Nanotechnol* **11**, 444 (2016).
28. Boule, O. et al. Room-temperature chiral magnetic skyrmions in ultrathin magnetic nanostructures. *Nat. Nanotechnol* **11**, 449 (2016).
29. Soumyanarayanan, A. et al. Tunable room-temperature magnetic skyrmions in Ir/Fe/Co/Pt multilayers. *Nat. Mater* **16**, 898 (2017).
30. Mandru, A.-O. et al. Coexistence of distinct skyrmion phases observed in hybrid ferromagnetic/ferrimagnetic multilayers. *Nat. Commun* **11**, 6365 (2020).
31. Zeissler, K. et al. Diameter-independent skyrmion Hall angle observed in chiral magnetic multilayers. *Nat. Commun* **11**, 428 (2020).
32. Birch, M. T. et al. Real-space imaging of confined magnetic skyrmion tubes. *Nat. Commun* **11**, 1726 (2020).
33. Fert, A., Cros, V. & Sampaio, J. Skyrmions on the track. *Nat. Nanotechnol* **8**, 152 (2013).
34. Sampaio, J., Cros, V., Rohart, S., Thiaville, A. & Fert, A. Nucleation, stability and current-induced motion of isolated magnetic skyrmions in nanostructures. *Nat. Nanotechnol* **8**, 839 (2013).
35. Tomasello, R. et al. A strategy for the design of skyrmion racetrack memories. *Sci. Rep* **4**, 6784 (2014).
36. Koshibae, W. et al. Memory functions of magnetic skyrmions. *Japan. J. Appl. Phys* **54**, 053001 (2015).
37. Yu, G. et al. Room-temperature creation and spin-orbit torque manipulation of skyrmions in thin films with engineered asymmetry. *Nano Lett* **16**, 1981 (2016).
38. Zhang, X., Zhou, Y. & Ezawa, M. Magnetic bilayer-skyrmions without skyrmion Hall effect. *Nat. Commun* **7**, 10293 (2016).
39. Zhang, X., Ezawa, M. & Zhou, Y. Thermally stable magnetic skyrmions in multilayer synthetic antiferromagnetic racetracks. *Phys. Rev. B* **94**, 064406 (2016).
40. Tomasello, R. et al. Performance of synthetic antiferromagnetic racetrack memory: domain wall versus skyrmion. *J. Phys. D: Appl. Phys* **50**, 325302 (2017).
41. Wang, Y. et al. Electric-field-driven non-volatile multi-state switching of individual skyrmions in a multiferroic heterostructure. *Nat. Commun* **11**, 3577 (2020).
42. Zhang, X., Ezawa, M. & Zhou, Y. Magnetic skyrmion logic gates: Conversion, duplication and merging of skyrmions. *Sci. Rep* **5**, 9400 (2015).
43. Luo, S. et al. Reconfigurable skyrmion logic gates. *Nano Lett* **18**, 1180 (2018).
44. Chauwin, M. et al. Skyrmion logic system for large-scale reversible computation. *Phys. Rev. Applied* **12**, 064053 (2019).
45. Mankalale, M. G., Zhao, Z., Wang, J.-P. & Sapatnekar, S. S. SkyLogic - A proposal for a skyrmion-based logic device. *IEEE Trans. Electron Devices* **66**, 1990 (2019).
46. Walker, B. W. et al. Skyrmion logic clocked via voltage-controlled magnetic anisotropy. *Appl. Phys. Lett* **118**, 192404 (2021).
47. Liang, X. et al. Antiferromagnetic skyrmion-based logic gates controlled by electric currents and fields. *Appl. Phys. Lett* **119**, 062403 (2021).
48. Zhang, X., Zhou, Y., Ezawa, M., Zhao, G. P. & Zhao, W. Magnetic skyrmion transistor: skyrmion motion in a voltage-gated nanotrack. *Sci. Rep* **5**, 11369 (2015).
49. Upadhyaya, P., Yu, G., Amiri, P. K. & Wang, K. L. Electric-field guiding of magnetic skyrmions. *Phys. Rev. B* **92**, 134411 (2015).
50. Hong, I.-S. & Lee, K.-J. Magnetic skyrmion field-effect transistors. *Appl. Phys. Lett* **115**, 072406 (2019).
51. Luo, S. et al. Voltage-controlled skyrmion memristor for energy-efficient synapse applications. *IEEE Electron Device Lett* **40**, 635 (2019).
52. Jiang, W. et al. Physical reservoir computing using magnetic skyrmion memristor and spin torque nano-oscillator. *Appl. Phys. Lett* **115**, 192403 (2019).
53. Huang, Y., Kang, W., Zhang, X., Zhou, Y. & Zhao, W. Magnetic skyrmion-based synaptic devices. *Nanotechnology* **28**, 08LT02 (2017).
54. Li, S. et al. Magnetic skyrmion-based artificial neuron device. *Nanotechnology* **28**, 31LT01 (2017).
55. Pinna, D. et al. Skyrmion gas manipulation for probabilistic computing. *Phys. Rev. Applied* **9**, 064018 (2018).
56. Prychynenko, D. et al. Magnetic skyrmion as a nonlinear resistive element: a potential building block for reservoir computing. *Phys. Rev. Applied* **9**, 014034 (2018).
57. Nozaki, T. et al. Brownian motion of skyrmion bubbles and its control by voltage applications. *Appl. Phys. Lett* **114**, 012402 (2019).
58. Zázvorka, J. et al. Thermal skyrmion diffusion used in a reshuffler device. *Nat. Nanotechnol* **14**, 658 (2019).
59. Song, K. M. et al. Skyrmion-based artificial synapses for neuromorphic computing. *Nat. Electron* **3**, 148 (2020).
60. Jibiki, Y. et al. Skyrmion Brownian circuit implemented in continuous ferromagnetic thin film. *Appl. Phys. Lett* **117**, 082402 (2020).
61. Zhang, X. et al. All-magnetic control of skyrmions in nanowires by a spin wave. *Nanotechnology* **26**, 225701 (2015).
62. Liu, Y. et al. Voltage-driven high-speed skyrmion motion in a skyrmion-shift device. *Phys. Rev. Applied* **11**, 014004 (2019).
63. Ma, C. et al. Electric field-induced creation and directional motion of domain walls and skyrmion bubbles. *Nano Lett* **19**, 353 (2019).
64. Jiang, W. et al. Direct observation of the skyrmion Hall effect. *Nat. Phys* **13**, 162 (2017).
65. Litzius, K. et al. Skyrmion Hall effect revealed by direct time-resolved X-ray microscopy. *Nat. Phys* **13**, 170 (2017).
66. Dohi, T., DuttaGupta, S., Fukami, S. & Ohno, H. Formation and current-induced motion of synthetic antiferromagnetic skyrmion bubbles. *Nat. Commun* **10**, 5153 (2019).
67. Rohart, S. & Thiaville, A. Skyrmion confinement in ultrathin film nanostructures in the presence of Dzyaloshinskii-Moriya interaction. *Phys. Rev. B* **88**, 184422 (2013).
68. Zhang, X., Zhou, Y. & Ezawa, M. High-topological-number magnetic skyrmions and topologically protected dissipative structure. *Phys. Rev. B* **93**, 024415 (2016).
69. Liu, Y., Du, H., Jia, M. & Du, A. Switching of a target skyrmion by a spin-polarized current. *Phys. Rev. B* **91**, 094425 (2015).
70. Beg, M. et al. Ground state search, hysteretic behaviour and reversal mechanism of skyrmionic textures in confined helimagnetic nanostructures. *Sci. Rep* **5**, 17137 (2015).
71. Zhang, B., Wang, W., Beg, M., Fangohr, H. & Kuch, W. Microwave-induced dynamic switching of magnetic skyrmion cores in nanodots. *Appl. Phys. Lett* **106**, 102401 (2015).
72. Zheng, F. et al. Direct imaging of a zero-field target skyrmion and its polarity switch in a chiral magnetic nanodisk. *Phys. Rev. Lett* **119**, 197205 (2017).
73. Lin, S.-Z. & Hayami, S. Ginzburg-Landau theory for skyrmions in inversion-symmetric magnets with competing interactions. *Phys. Rev. B* **93**, 064430 (2016).
74. Zhang, X. et al. Skyrmion dynamics in a frustrated ferromagnetic film and current-induced helicity locking-unlocking transition. *Nat. Commun* **8**, 1717 (2017).
75. Xia, J. et al. Current-driven dynamics of frustrated skyrmions in a synthetic antiferromagnetic bilayer. *Phys. Rev. Applied* **11**, 044046 (2019).
76. Zhang, X. et al. Static and dynamic properties of bimerons in a frustrated ferromagnetic monolayer. *Phys. Rev. B* **101**, 144435 (2020).
77. Xia, J. et al. Current-driven skyrmionium in a frustrated magnetic system. *Appl. Phys. Lett* **117**, 012403 (2020).
78. Zhang, X. et al. A frustrated bimeronium: Static structure and dynamics. *Appl. Phys. Lett* **118**, 052411 (2021).
79. Lin, S.-Z., Batista, C. D. & Saxena, A. Internal modes of a skyrmion in the ferromagnetic state of chiral magnets. *Phys. Rev. B* **89**, 024415 (2014).
80. Khanh, N. D. et al. Nanometric square skyrmion lattice in a centrosymmetric tetragonal magnet. *Nat. Nanotechnol* **15**, 444 (2020).
81. Hayami, S. & Motome, Y. Square skyrmion crystal in centrosymmetric itinerant magnets. *Phys. Rev. B* **103**, 024439 (2021).
82. Peng, L. et al. Controlled transformation of skyrmions and antiskyrmions in a non-centrosymmetric magnet. *Nat. Nanotechnol* **15**, 181 (2020).
83. Xia, J. et al. Dynamics of an elliptical ferromagnetic skyrmion driven by the spin-orbit torque. *Appl. Phys. Lett* **116**, 022407 (2020).
84. Jena, J. et al. Elliptical Bloch skyrmion chiral twins in an antiskyrmion system. *Nat. Commun* **11**, 1115 (2020).
85. Cui, B. et al. Néel-Type Elliptical Skyrmions in a Laterally Asymmetric Magnetic Multilayer. *Adv. Mater* **33**, 2006924 (2021).
86. Ma, F., Reichhardt, C., Gan, W., Reichhardt, C. J. O. & Lew, W. S. Emergent geometric frustration of artificial magnetic skyrmion crystals. *Phys. Rev. B* **94**, 144405 (2016).
87. Juge, R. et al. Helium ions put magnetic skyrmions on the track. *Nano Lett* **21**, 2989 (2021).
88. Ohara, K. et al. Confinement and protection of skyrmions by patterns of modified magnetic properties. *Nano Lett* **21**, 4320 (2021).
89. Reichhardt, C. & Reichhardt, C. J. O. Switching and jamming transistor effect for vortex matter in honeycomb pinning arrays with ac drives. *Phys. Rev. B* **81**, 024510 (2010).
90. Reichhardt, C., Ray, D. & Reichhardt, C. J. O. Collective transport properties of driven skyrmions with random disorder. *Phys. Rev. Lett* **114**, 217202 (2015).

91. Reichhardt, C., Ray, D. & Reichhardt, C. J. O. Quantized transport for a skyrmion moving on a two-dimensional periodic substrate. *Phys. Rev. B* **91**, 104426 (2015).
92. Reichhardt, C. & Reichhardt, C. J. O. Shapiro steps for skyrmion motion on a washboard potential with longitudinal and transverse ac drives. *Phys. Rev. B* **92**, 224432 (2015).
93. Reichhardt, C., Ray, D. & Reichhardt, C. J. O. Magnus-induced ratchet effects for skyrmions interacting with asymmetric substrates. *New J. Phys* **17**, 073034 (2015).
94. Reichhardt, C. & Reichhardt, C. J. O. Noise fluctuations and drive dependence of the skyrmion Hall effect in disordered systems. *New J. Phys* **18**, 095005 (2016).
95. Reichhardt, C. & Reichhardt, C. J. O. Magnus-induced dynamics of driven skyrmions on a quasi-one-dimensional periodic substrate. *Phys. Rev. B* **94**, 094413 (2016).
96. Müller, J. Magnetic skyrmions on a two-lane racetrack. *New J. Phys* **19**, 025002 (2017).
97. Reichhardt, C., Ray, D. & Reichhardt, C. J. O. Nonequilibrium phases and segregation for skyrmions on periodic pinning arrays. *Phys. Rev. B* **98**, 134418 (2018).
98. Fernandes, I. L., Bouaziz, J., Blügel, S. & Lounis, S. Universality of defect-skyrmion interaction profiles. *Nat. Commun* **9**, 4395 (2018).
99. Menezes, R. M., Mulkers, J., de Souza Silva, C. C. & Milosevic, M. V. Deflection of ferromagnetic and antiferromagnetic skyrmions at heterochiral interfaces. *Phys. Rev. B* **99**, 104409 (2019).
100. González-Gómez, L., Castell-Queralt, J., Del-Valle, N., Sanchez, A. & Navau, C. Analytical modeling of the interaction between skyrmions and extended defects. *Phys. Rev. B* **100**, 054440 (2019).
101. Castell-Queralt, J., González-Gómez, L., Del-Valle, N., Sanchez, A. & Navau, C. Accelerating, guiding, and compressing skyrmions by defect rails. *Nanoscale* **11**, 12589 (2019).
102. Bhatti, S. & Piramanayagam, S. N. Effect of Dzyaloshinskii-Moriya interaction energy confinement on current-driven dynamics of skyrmions. *Phys. Status Solidi RRL* **13**, 1900090 (2019).
103. Reichhardt, C. & Reichhardt, C. J. O. Shear banding, intermittency, jamming, and dynamic phases for skyrmions in inhomogeneous pinning arrays. *Phys. Rev. B* **101**, 054423 (2020).
104. Vizir, N. P., Reichhardt, C., Venegas, P. A. & Reichhardt, C. J. O. Shapiro steps and nonlinear skyrmion Hall angles for dc and ac driven skyrmions on a two-dimensional periodic substrate. *Phys. Rev. B* **102**, 104413 (2020).
105. Feilhauer, J. et al. Controlled motion of skyrmions in a magnetic antidot lattice. *Phys. Rev. B* **102**, 184425 (2020).
106. Fernandes, I. L., Chico, J. & Lounis, S. Impurity-dependent gyrotropic motion, deflection and pinning of current-driven ultrasmall skyrmions in PdFe/Ir(111) surface. *J. Phys.: Condens. Matter* **32**, 425802 (2020).
107. Arjana, I. G., Fernandes, I. L., Chico, J. & Lounis, S. Sub-nanoscale atom-by-atom crafting of skyrmion-defect interaction profiles. *Sci. Rep* **10**, 14655 (2020).
108. Chen, W., Liu, L. & Zheng, Y. Ultrafast ratchet dynamics of skyrmions by defect engineering in materials with poor conductivity under gigahertz magnetic fields. *Phys. Rev. Appl* **14**, 064014 (2020).
109. Vizir, N. P., Bellizzi Souza, J. C., Reichhardt, C., Reichhardt, C. J. O. & Venegas, P. A. Directional locking and the influence of obstacle density on skyrmion dynamics in triangular and honeycomb arrays. *J. Phys.: Condens. Matter* **33**, 305801 (2021).
110. Coppersmith, S. N., Fisher, D. S., Halperin, B. I., Lee, P. A. & Brinkman, W. F. Dislocations and the commensurate-incommensurate transition in two dimensions. *Phys. Rev. B* **25**, 349 (1982).
111. Harada, K. et al. Direct observation of vortex dynamics in superconducting films with regular arrays of defects. *Science* **274**, 1167 (1996).
112. Martín, J. I., Vélez, M., Nogués, J. & Schuller, I. K. Flux pinning in a superconductor by an array of submicrometer magnetic dots. *Phys. Rev. Lett* **79**, 1929 (1997).
113. Reichhardt, C., Olson, C. J. & Nori, F. Commensurate and incommensurate vortex states in superconductors with periodic pinning arrays. *Phys. Rev. B* **57**, 7937 (1998).
114. Berdiyrov, G. R., Milosevic, M. V. & Peeters, F. M. Novel commensurability effects in superconducting films with antidot arrays. *Phys. Rev. Lett* **96**, 207001 (2006).
115. Tung, S., Schweikhard, V. & Cornell, E. A. Observation of vortex pinning in bose-einstein condensates. *Phys. Rev. Lett* **97**, 240402 (2006).
116. Bohlein, T., Mikhael, J. & Bechinger, C. Gradient-index meta-surfaces as a bridge linking propagating waves and surface waves. *Nat. Mater* **11**, 126 (2012).
117. de Jong, M. C. H. et al. Local control of magnetic interface effects in chiral Ir|Co|Pt multilayers using Ga⁺ ion irradiation, *arXiv:2110.01424* (2021).
118. Donahue, M. J. and Porter, D. G. Interagency Report NO. NISTIR 6376, National Institute of Standards and Technology, Gaithersburg, MD (1999) [<http://math.nist.gov/oommf/>].

Acknowledgements

X.Z. was an International Research Fellow of the Japan Society for the Promotion of Science (JSPS). X.Z. was supported by JSPS KAKENHI (Grant No. JP20F20363). O.A.T. acknowledges the support by the Australian Research Council (Grant No. DP200101027), NCMAS grant, and the Cooperative Research Project Program at the Research Institute of Electrical Communication, Tohoku University. M.E. acknowledges the support by the Grants-in-Aid for Scientific Research from JSPS KAKENHI (Grant Nos. JP17K05490 and JP18H03676) and the support by CREST, JST (Grant Nos. JPMJCR16F1 and JPMJCR20T2). Y.Z. acknowledges the support by the Guangdong Special Support Project (Grant No. 2019BT02X030), Shenzhen Fundamental Research Fund (Grant No. JCYJ20210324120213037), Shenzhen Peacock Group Plan (Grant No. KQTD20180413181702403), Pearl River Recruitment Program of Talents (Grant No. 2017GC010293), and National Natural Science Foundation of China (Grant Nos. 11974298 and 61961136006). X.L. acknowledges the support by the Grants-in-Aid for Scientific Research from JSPS KAKENHI (Grant Nos. JP20F20363, JP21H01364, and JP21K18872).

Author contributions

X.L. and X.Z. conceived the idea. X.L., M.E., and Y.Z. coordinated the project. X.Z. and J.X. performed the computational simulations and data analysis. M.E. and O.A.T. carried out the theoretical analysis. X.Z. drafted the manuscript and revised it with input from J.X., K.S., H.F., M.E., O.A.T., Y.Z., and X.L. All authors discussed the results and reviewed the manuscript. X.Z. and J.X. contributed equally to this work.

Competing interests

The authors declare no competing interests.

Additional information


Supplementary information The online version contains supplementary material available at <https://doi.org/10.1038/s42005-021-00761-7>.

Correspondence and requests for materials should be addressed to Motohiko Ezawa, Yan Zhou or Xiaoxi Liu.

Peer review information *Communications Physics* thanks Max Birch and the other, anonymous, reviewer(s) for their contribution to the peer review of this work. Peer reviewer reports are available.

Reprints and permission information is available at <http://www.nature.com/reprints>

Publisher's note Springer Nature remains neutral with regard to jurisdictional claims in published maps and institutional affiliations.

 **Open Access** This article is licensed under a Creative Commons Attribution 4.0 International License, which permits use, sharing, adaptation, distribution and reproduction in any medium or format, as long as you give appropriate credit to the original author(s) and the source, provide a link to the Creative Commons license, and indicate if changes were made. The images or other third party material in this article are included in the article's Creative Commons license, unless indicated otherwise in a credit line to the material. If material is not included in the article's Creative Commons license and your intended use is not permitted by statutory regulation or exceeds the permitted use, you will need to obtain permission directly from the copyright holder. To view a copy of this license, visit <http://creativecommons.org/licenses/by/4.0/>.

© The Author(s) 2021